

Effect of Material Chemical Composition on the Formation of Halo Ring in a Gen 3 Q&P 980 Steel

Dileep Chandran Ramachandran ^{a,1}, Adib Salandari-Rabori ^a, Andrew Macwan ^b, Elliot Biro ^a

^a Centre for Advanced Materials Joining, Department of Mechanical & Mechatronics Engineering,
University of Waterloo, Waterloo, Ontario N2L 3G1, Canada.

^b ArcelorMittal Global Research, 1390 Burlington Street East, Hamilton, ON L8N 3J5, Canada.

¹ Corresponding author: *Dileep Chandran Ramachandran*

Centre for Advanced Materials Joining, Department of Mechanical & Mechatronics Engineering,

University of Waterloo, Waterloo, Ontario, Canada N2L 3G1

E-mail: dramachandran@uwaterloo.ca

Abstract

This study investigates how fusion zone (FZ) chemical composition influences the formation of the halo ring, a transient softening region that can form along the fusion boundary (FB) of resistance spot welds in Q&P980. For this purpose, spot welds were made in both similar Q&P steel joints as well as joints sandwiching low carbon (LC) or high carbon (HC) steels with Q&P steels, which tailored the chemical composition of the FZ. Electron probe microanalysis (EPMA) characterization was performed on a spot-welded sample to understand the effect of material chemical composition on the halo formation. Alloying elements such as C, Mn, and Si were significantly less in the FZ composition of the welds made with LC steel, as compared to 3-sheet Q&P weld, which resulted in associated 33% reduction in hardness of the LC steel FZ. On the contrary, the C and Mn were higher in the FZ of the weld made with HC steel compared to that of the 3-sheet Q&P weld. However, like the welds made with the LC steel the FZ of the welds with the HC steel had a lower Si content than the FZ of the 3-sheet Q&P steel. The increase in C and Mn contents in the welds made with the HC steel resulted in an 14% increase in FZ hardness compared to the FZ of the 3-sheet Q&P steel. The halo formation is more prominent in welds made with LC steel. It was wider in welds where the FZ had a lower alloy content than the Q&P steel as compared to the higher alloyed FZ of the weld made with the HC steel. In LC steel weld a high Mn and Si segregated region inside the FZ was also observed. It was shown that the transient softened zone can be affected by the difference in chemical composition between the FZ and heat-affected zone (HAZ). Therefore, any changes in mechanical properties associated with the halo are more likely to be more prominent in dissimilar welds where high and low alloy steels are combined.

Keywords: Advanced High Strength Steels; Resistance Spot Welding; Halo Ring; Microstructure

1. Introduction

The use of quenched and partitioned (Q&P) steel ^[1], one of the third-generation advanced high-strength steels (3G-AHSS), has garnered significant interest for application in auto body structures, owing to its impressive blend of strength and ductility ^[1,2]. In the manufacturing process of auto body-in-white (BIW) structures, Q&P steels find frequent use in key structural elements like longitudinal beams and reinforcements for B-pillars ^[3]. The main joining method extensively employed in the manufacturing of BIWs is resistance spot welding (RSW), primarily due to cost-effectiveness and efficient high-volume production ^[4]. However, the RSW of Q&P steel is not well understood considering the higher concentration of alloying elements in this type of steel which can segregate on the fusion boundary (FB) and trigger a favorable path for crack propagation ^[5-8].

An automotive body typically contains five thousand spot-welds in its body-in-white structures ^[9]. These weld joints contain similar or dissimilar combinations of sheet steels, which play a crucial role in the crashworthiness of the structure ^[10]. Welding dissimilar materials demands greater precautions compared to the conventional welding of similar steel combinations since the welding thermal cycle destroys the engineered multiphase microstructures ^[11]. This is due to potential differences in thickness, thermal conductivity, melting points, and even coating types between the steels being joined ^[12-14]. The primary challenges of a RSW process arise from the intricate interplay of chemical and physical factors, such as fusion zone (FZ) composition and heat input, respectively, that come into play during the joining of the sheets ^[15,16].

The weldability of Q&P steels is a key factor for the application of this steel grade in the automotive industry. Pouranvari et al. ^[17] reported that the mechanical performance of the RSW predominantly depends on the failure location in the welds during the application of strain. Previous studies ^[8,18-22] showed that failure in welds made without care to optimize process parameters often failed along a local soft area in the FB, known as the halo ring. The formation of the halo ring in RSW is a result of thermal and metallurgical processes that occur during the welding ^[6,8]. The halo ring region is considered a depleted C, Mn, and Si zone in the resistance spot welds ^[8,18]. It is believed that these elements have diffused from the halo ring to the FZ. Due to the depleted C, Mn, and Si in the halo ring, the austenite transforms into upper bainite, as reported in our previous study ^[23]. Amirthalingam et al. ^[24] showed that the solidification of the

weld pool progresses with a strong partitioning of carbon and phosphorous to the unsolidified liquid. Which was cited as the primary reason for the lower level of carbon at the FB. Furthermore, Zhang et al. [3] reported that Si and Mn that were present in the AHSS, generally segregated on the grain boundaries during welding. This segregation led to the activation of stress concentration sites at grain boundaries resulting in the reduction of weld strength. Taniguchi et al. [19] also concluded that the depletion of Mn from the fusion boundary leads to the depletion of hardness, which eventually acts as a crack propagation path during loading. The authors' previous study showed that implementing a double-pulse welding schedule [8] and post-weld heat treatment such as paint baking [18,25] homogenizes the elements in the FB, leading to the full or partial elimination of the halo region in two Q&P steel sheet combination. Similar findings were also reported by Manladan et al. [20]. However, in automotive body manufacturing, welds typically involve various sheet combinations, and these diverse steel combinations may influence the formation of the halo ring. To clarify, the diffusion of C, Mn, and Si towards the halo ring depends on the chemical composition of the steel sheets being used [18]. Only a limited number of studies have been conducted on the weldability of Q&P steels in similar and dissimilar configurations. The spot welding of Q&P steels with diverse steel combinations requires rigorous control of the joining parameters to achieve a suitable mechanical strength and energy absorption capability for the automotive industry [26].

Despite considerable efforts to elucidate the mechanical behavior and failure mechanisms in resistance spot welds of Q&P 980 steel, there remains a notable gap in understanding the influence of material composition on the microstructural evolution of the weld nugget and surrounding HAZ. Additionally, due to limitations in the size of the halo ring, prolonged welding times with a welding current nearly at the far end of the weld lobe were employed to enhance halo ring formation [27,28]. This research focuses on providing insights into the microstructural characteristics of 1.2 mm thick Q&P 980 steel sandwiched between low-carbon mild steel and high-carbon steel with thicknesses of 1.5 mm and 1.4 mm, respectively. To bridge the existing knowledge deficit, the investigation explores the impact of steel chemistry on the microstructural changes in the nugget, HAZ, and halo ring, employing advanced characterization techniques such as electron probe micro-analysis and electron back-scattered diffraction (EBSD). This study is crucial for advancing our understanding of the intricate relationships between material composition and microstructural evolution in Q&P

steel resistance spot welds, providing valuable insights for optimizing welding processes in the automotive industry.

2. Materials and Methods

2.1 Material

This study examines experimental Zn-coated 1.2 mm thick Q&P 980 steel with a nominal chemical composition of 0.23 wt.% C, and other alloying elements, as shown in Table 1. The carbon equivalent of the material is 0.65 and was calculated according to the formula proposed by Yurioka et al. ^[29] (see Equations 1 and 2). A 1.5 mm low C (denoted as LC) steel and a 1.4 mm high C (denoted as HC) steel were also used in this study, and their nominal chemical composition also is given in Table 1.

$$C_{eq} = C + A(C) \cdot \left\{ \frac{Si}{24} + \frac{Mn}{6} + \frac{Cu}{20} + \frac{Ni}{20} + \frac{Cr+Mo+Nb+V}{5} + 5B \right\} \quad (1)$$

$$\text{Where } A(c) = 0.75 + 0.25 \tanh\{20(C - 0.12)\} \quad (2)$$

Table 1: Chemical composition (in wt.%) of the steel used in this study.

	C	Mn	Si	Cr+Mo+Ti+Nb	CE
Q&P 980 steel	0.2	2.0	1.1	0.22	0.65
LC steel	0.002	0.08	0.004	0.08	0.01
HC steel	0.4	0.6	0.6	0.57	0.69

The microstructure of the as-received steel consists of a combination of ferrite (F), martensite (M), tempered martensite (TM), and retained austenite (RA), as shown in Fig. 1a, and b. A detailed microstructural analysis was reported in our previous studies ^[8,18].

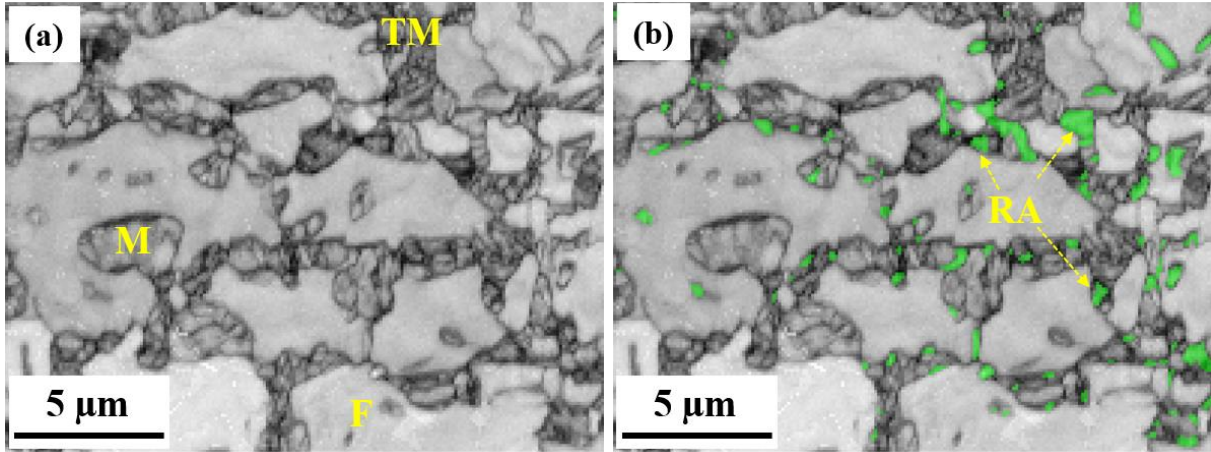


Fig. 1: EBSD map of as-received Q&P 980 steel. (a) Image quality map, and (b) phase map.

2.2 Resistance Spot Welding

The RSW process was carried out using a medium-frequency direct current (MFDC) robot with a C-type transformer (servo gun) and a Rexroth Bosh weld controller. The welding schedules were primarily chosen according to the AWS D8.9 specifications^[30]. The cooling water flow rate was $4 \text{ L}\cdot\text{min}^{-1}$. A dome-shaped Cu-Cr electrode with a flat face diameter of 6 mm was used for the welding. Moreover, the sample surfaces were cleaned with alcohol before the welding to remove the contaminations. Other welding parameters used in this study are shown in Table 2 and Fig. 2. This study employed extended welding schedules, in which the welding time is longer than the AWS-recommended^[31] schedule for a similar two-sheet combination of 1.2 mm Q&P 980 steels. An electrode force of 4 kN was used in all the experimented conditions. The samples were welded 0.2 kA below the expulsion current. The average nugget diameter of all the conditions is shown in Table 2.

Table 2: Welding parameters used in this study and the corresponding nugget diameters.

	Welding time (ms)	Welding current (kA)	ND (mm)
Q&P 980 steel	470	9.5	7.29
LC steel weld	470	9.8	6.96
HC steel weld	470	9.6	7.11

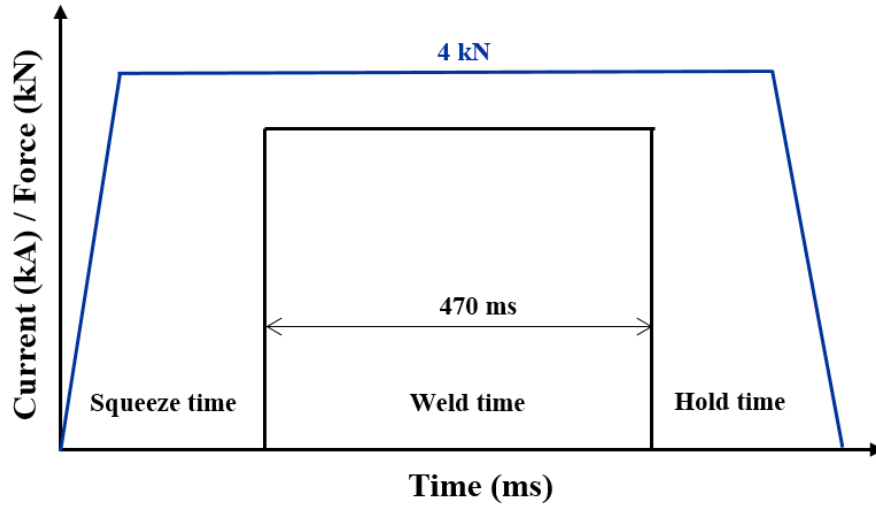


Fig. 2: Schematic diagram showing the welding schedule used in this study.

2.3 Microstructural Characterization

For metallographic analysis, the samples were prepared by conventional metallographic techniques. They were polished up to a 1 μm diamond finish followed by etching with 2% Nital solution for 10 s. Optical (Olympus BX51M) and scanning electron microscopy (Zeiss UltraPlus FE-SEM) were used to characterize the microstructure. A JEOL JSM 7000F field emission SEM interfaced with an EBSD detector was used to characterize the microstructure. An Aztec crystal software was used for the EBSD data post-processing. The elements and their distribution along the FB were determined using an electron probe microanalysis (FE-EPMA; JEOL JXA-8530F). The EPMA maps were performed with a 1 μm step size and a 100 ms dwell time, whereas the quantified line scans were done with a 1 μm step size and a 10 s dwell time.

2.4 Microhardness

Hardness measurements were performed on unetched samples using an automated Clemex microhardness machine interfaced with a Vickers indenter. Hardness line scans were performed using a 0.2 kgf load and a dwell time of 10 s. The spacing between the consecutive indents was kept constant at 150 μm . The high-density hardness scans were performed with a load of 0.005 kgf with an average spacing of 50 μm . The error bars of the average microhardness represent the 95% confidence interval.

3. Results and Discussion

3.1. Microstructural Characterization

The cross-sectional micrographs illustrating the microstructure of the 3-sheet Q&P combination, sandwich weld made with LC steel (LC steel weld), and sandwich weld made with HC steel (HC steel weld) combination are shown in Fig. 3a-c. As can be seen in Fig. 3, the nugget shapes are rectangular. The weld nugget formation is a balance between heat generation and heat dissipation, which is a function of the welding schedule, steel sheet combination, sheet thickness, and heat conductivity ^[10]. Gould et al. ^[32] reported that the cooling rate in RSW varies, ranging from $10 \times 10^5 \text{C/s}$ for a sheet thickness less than 0.5 mm to approximately $2 \times 10^3 \text{C/s}$ for a sheet thickness of 2.0 mm. It is noteworthy that, despite minor differences in welding current depending on the steel combination, the welding parameters are kept constant in all three conditions. The microstructure of the nugget in all three scenarios is characterized by columnar dendrites, indicative of a rapid cooling rate.

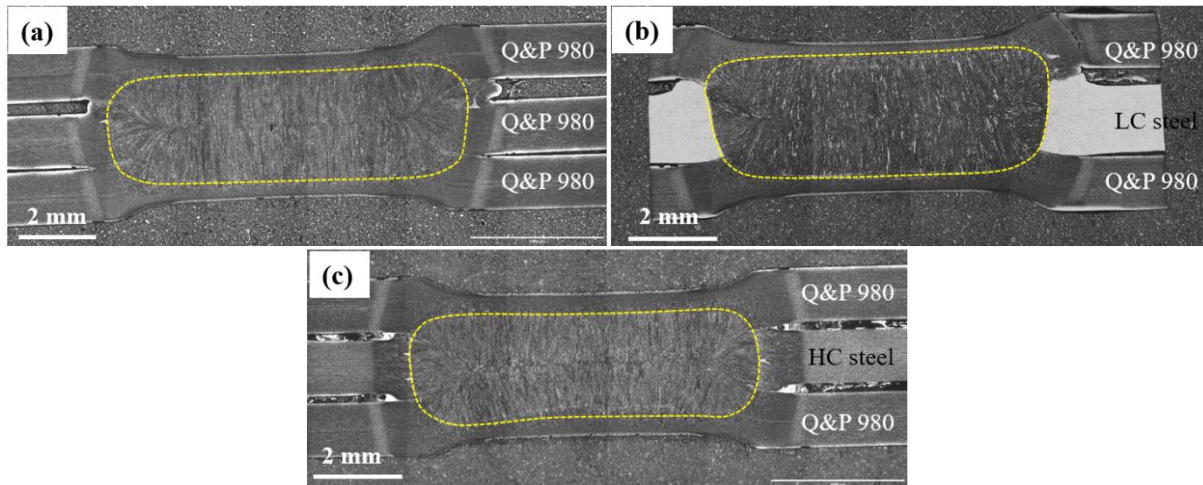


Fig. 3: Optical microstructure of (a) 3-sheet Q&P 980 (b) LC steel weld, and (c) HC steel weld

Detailed microstructural analysis of both the FZ and HAZ is crucial for gaining insights into the quality of spot welds. The microstructures observed in the FZ and upper critical heat affected zone (UCHAZ) of the 3-sheet Q&P steel configuration closely resemble those found in the two-sheet Q&P steel combinations, as reported in our prior study ^[8]. In both the FZ and the UCHAZ, the predominant constituents are lath martensite, and block martensite, respectively ^[8,18]. On the

contrary, the LC steel sandwich exhibits a combination of martensite, Widmanstätten (side-plate) ferrite, and grain boundary ferrite (allotriomorphic ferrite) microstructures, as shown in Fig. 4. From the IQ map of the LC steel sandwich (Fig. 4a), both ferrite (body-centered cubic-BCC structure) and martensite (body-centered tetragonal-BCT structure) phases are visible. The darker appearance of the martensite phases is attributed to their higher dislocation density, signifying higher lattice distortion compared to the ferrite. Fig. 4b illustrates the inverse pole figure (IPF) map of the weld, indicating the directional solidification structure aligned with the direction of the highest cooling rate. Within the FZ, distinct micrographs depict the presence of ferrite side-plates and grain boundary ferrite, as seen in Fig. 4c and d, respectively. The characterization of these microstructures was conducted based on their morphologies ^[33]. It is noteworthy that the FZ microstructure reveals a relatively significant volume of ferrite morphologies, particularly ferrite side-plates, whereas the UHAZ, the Q&P steel side exhibits coarse packets of martensite, while the LC steel side is predominantly ferritic.

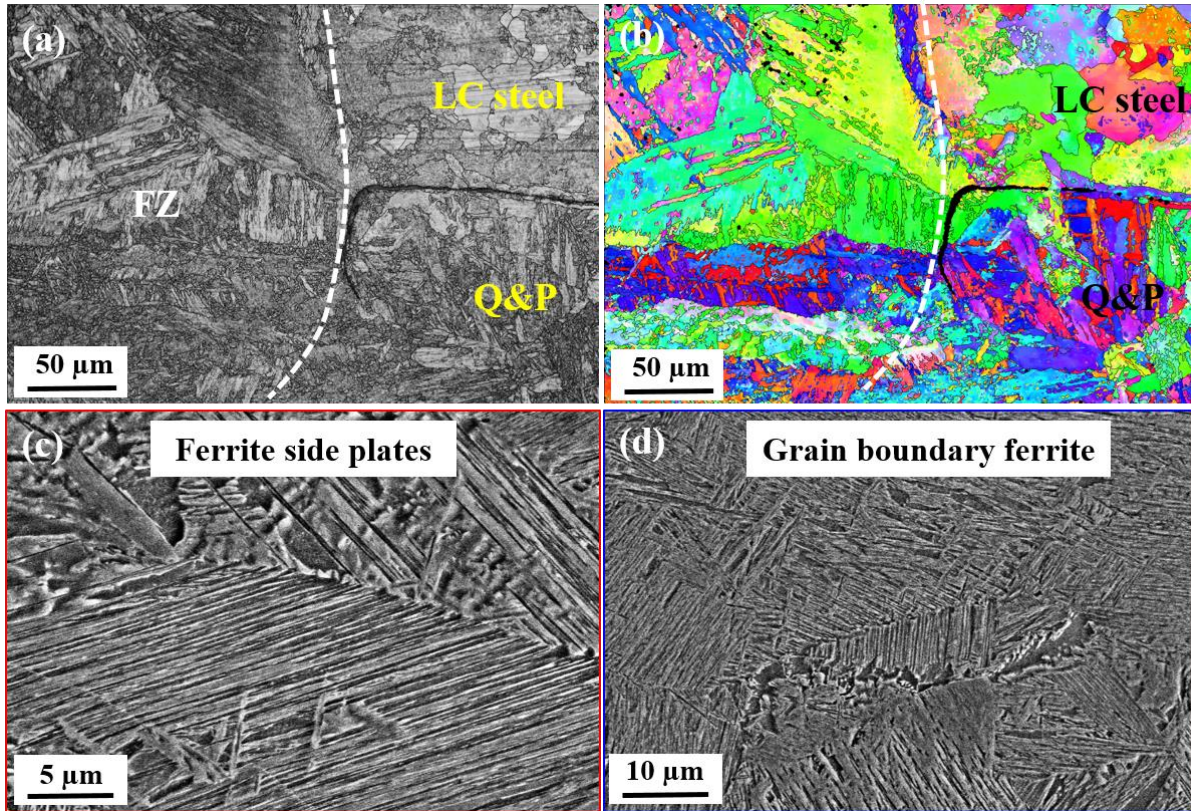


Fig. 4: A typical EBSD microstructure of FZ and HAZ of the two-sheet Q&P and LC Steels combination: (a) IQ map, (b) IPF map, (c and d) FZ microstructure showing different ferrite morphologies; side-plate and grain boundary ferrite, respectively.

A typical EBSD micrograph of the HC steel sandwich weld is shown in Fig. 5a. The IQ map reveals the Q&P steel on the top and the HC steel in the middle of the 3-sheet stackups. The IPF map shown in Fig. 5b indicates the FZ microstructure shares a similar texture with UCHAZ. This also implies that both microstructures are similar, mainly martensitic, and the only difference lies in the martensite morphology. The higher carbon content in the FZ compared to the LC steel case facilitates the formation of martensite in the HC steel weld. The FZ microstructure shows a lath martensitic structure (see Fig. 5c). The IQ map depicts that there is no ferrite (relatively low dislocation density) microstructure in the characterized area. It is also worth noting that the UCHAZ of the HC steel consists of a comparatively smaller grain size than the Q&P steel side.

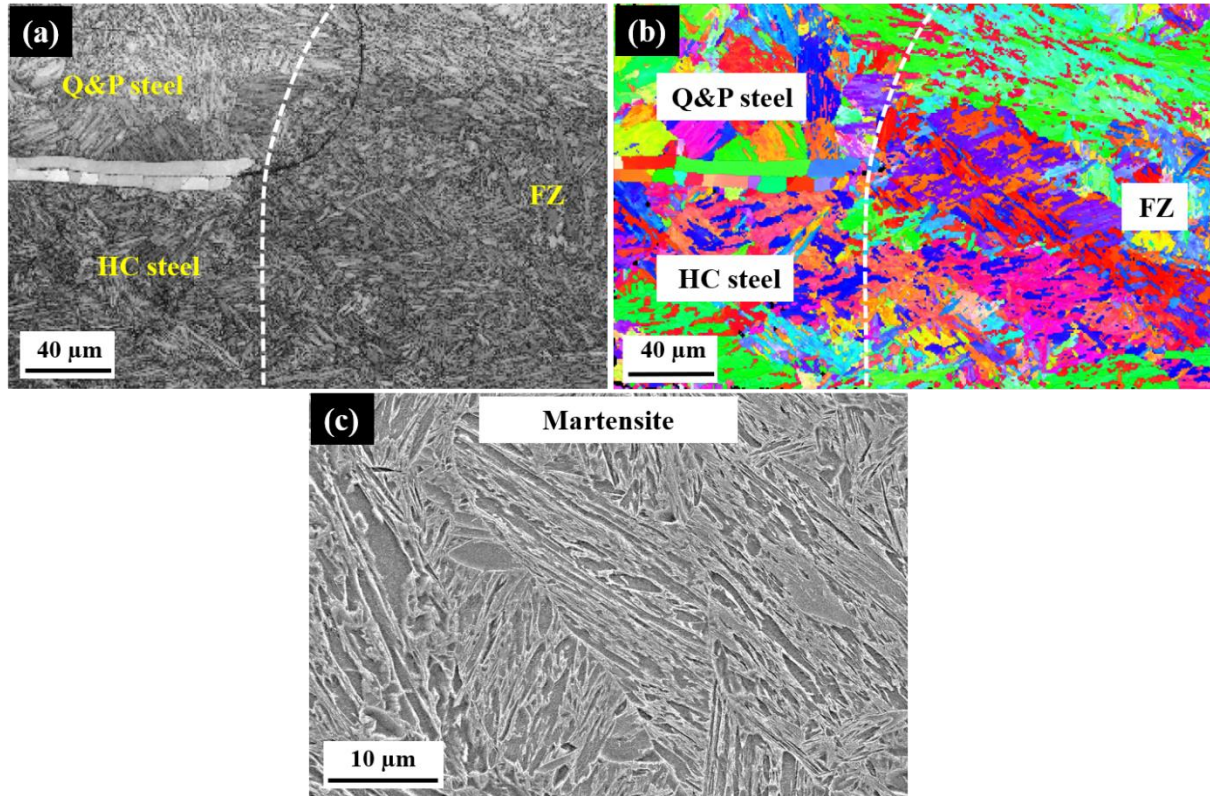


Fig. 5: A typical EBSD micrograph of weld made with HC steel showing FZ and HAZ. (a) IQ map, (b) IPF map, and (c) FZ microstructure showing a lath martensite morphology.

3.2. Hardness Analysis

The measured cross-weld hardness profile from base metal to FZ in different Q&P steel sheet stack-ups is shown in Fig. 6. For consistency, hardness analysis was only conducted on the Q&P steel side of the joint (see Fig. 6a). As shown in Fig. 6b, the FZ hardness increased to 570 HV in the case of the HC steel sandwiched between the two Q&P steels. Similarly, the FZ hardness significantly decreased to 372 HV when alloyed with LC steel. This observation is in good agreement with the observed FZ microstructure, where ferrite side-plate and grain boundary ferrite structures were observed in the FZ of LC steel sandwich weld. It is also important to note that spot welding with the HC steel increases the presence of high-carbon martensite which in turn increases the FZ hardness. Moreover, within each dissimilar weld, the hardness was quite constant along the Q&P steel HAZ implying a similar microstructure along the HAZ in all stack-up combinations. Furthermore, in the HC steel case, there is a slight increase in the hardness near the base material (at HAZ/BM interface) which is elaborated in the following section.

The high-density hardness analysis along the FB region of the Q&P steel side on all three combinations is shown in Fig. 6c. Softening in the FB is visible in all three combinations, namely, the halo region. The extent of softening can be measured by introducing the “degree of softening” parameter, the ratio of the difference in hardness between the halo ring and the hardness of the surrounding microstructure (HAZ). The degree of softening of all three combinations is calculated and shown in Fig. 6d. The degree of softening gives a clear understanding of the severity of the halo ring. For instance, the 3-sheet Q&P steel combination has a 19% reduction in halo ring hardness compared to the hardness of the UCHAZ (since the average hardness of the UCHAZ is similar in all the conditions). Similarly, LC steel and HC steel weld conditions have 46% and 16% reduction in hardness compared to the no halo condition, respectively. It can be seen from Fig. 6d that the LC steel weld combination has the highest and the HC steel combination has the lowest severity of halo, respectively. It can be seen from Fig. 6c that the hardness of the HAZ does not reach a consistent value across different weld combinations. Moreover, the reduction in hardness at the halo ring is directly related to the distribution of alloying elements on it. Further explanation regarding the differences in alloying elements within the halo ring will be provided subsequently.

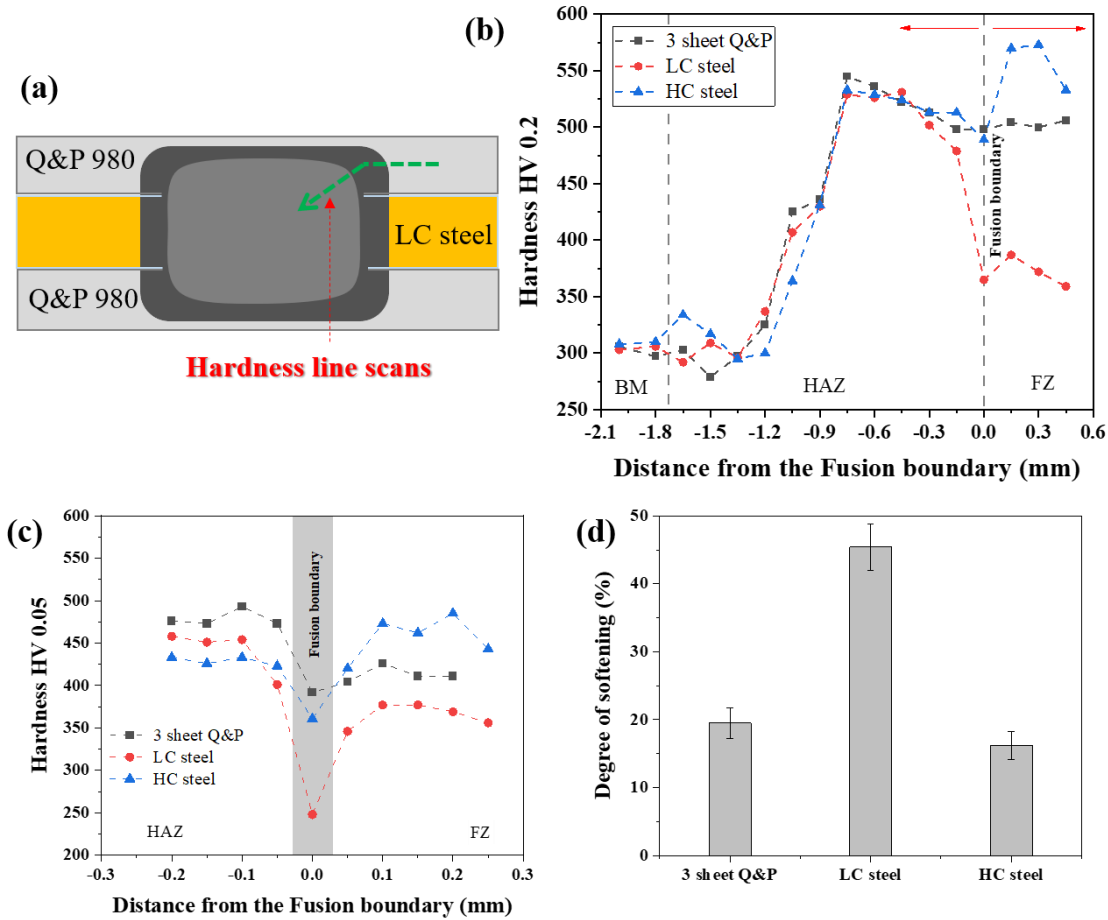


Fig. 6: (a) Schematic diagram showing the position of hardness analysis, (b) hardness profile of the three combinations, (c) high-density hardness along the FB, (d) degree of softening.

3.3. Elemental Distribution

The elemental distribution at the FB is an important factor in defining the halo ring in all three combinations. For this purpose, a comprehensive EPMA study was conducted on the samples focusing on the FB. EPMA results of similar combinations of the two-sheet Q&P steel spot welds were reported in our previous study [8] where a carbon-depleted region was found near the FB, closer to the fusion zone side. Moreover, a segregation of Mn and Si near the FB, closer to the HAZ side was also observed. Fig. 7 shows the elemental distribution map of the 3-sheet Q&P steel weld. Elemental maps of C, Si, and Mn are shown in Fig. 7b-d, respectively. It can be seen there is no significant difference in C, Si, and Mn concentration between the FZ and the HAZ in the

Q&P 3-sheet stack-up. This could be due to a comparatively wider scanning area compared to the width of the halo ring. However, close observation shows that there is a slight reduction in C content at the FB of the top Q&P steel in the stack up (see Fig. 7b). The segregation of Si and Mn on the inter-dendritic region can be seen from Fig. 7c and d. Eftekharmilani et al. [34] reported that during solidification the elements such as Mn, Si, and P tend to segregate at the inter-dendritic region due to their preferential partitioning behavior. Although the solidification process can potentially draw more solute Mn and Si towards the molten weld pool from the solid HAZ in a 3-sheet Q&P weld, the composition of the FZ and the welding schedule employed in this case do not facilitate this phenomenon. Therefore, there is no significant depletion of Si and Mn observed in the halo of the 3-sheet Q&P stack-up at these welding conditions.

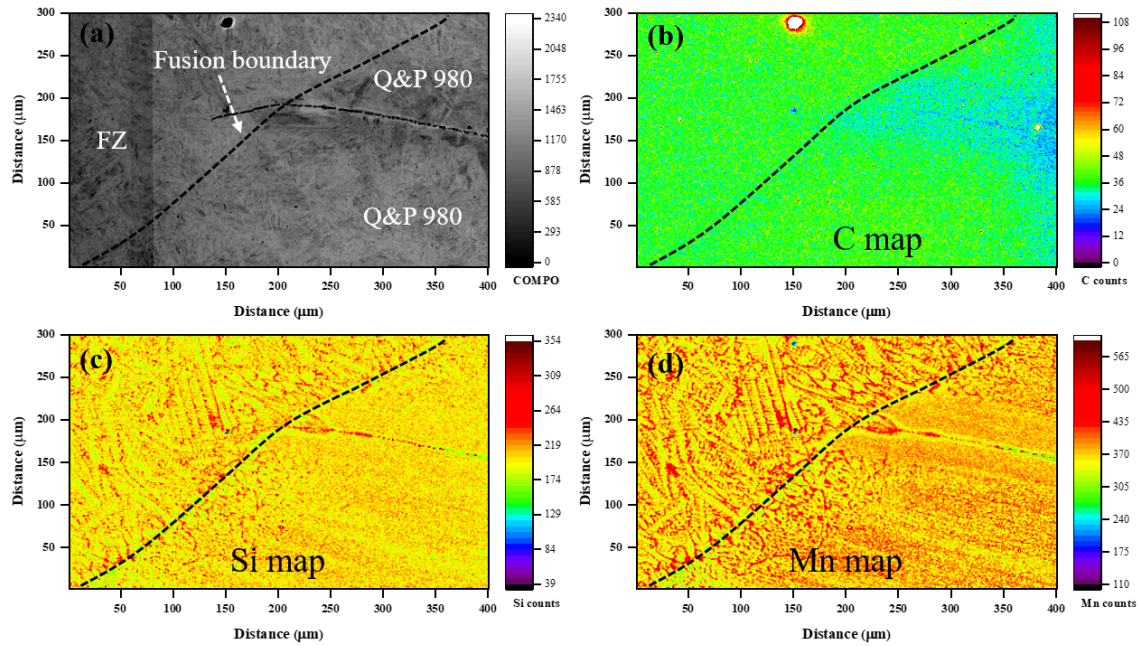


Fig. 7: 3-sheet Q&P steel stack-up, (a) SEM backscatter (BSE) image; Elemental distribution map: (b) Carbon, (c) Silicon, and (d) Manganese.

The elemental distribution map of the LC steel stack-up weld is shown in Fig. 8. The BSE image of the interface between Q&P and LC steel is shown in Fig. 8a. In Fig. 8b, the EPMA map highlights a strong depletion of C near the FB. Notably, the C-depleted region extends approximately 75 μm from the FB (see white arrows in Fig. 8b) and is within the HAZ side of the FB. Additionally, the carbon content of both the FZ and the halo region is comparable to each

other and lower than that of the Q&P steel base metal. It should be noted that the overall carbon content decreased in the FZ due to the mixing of lower alloyed IF steel with Q&P steel, which has a comparatively higher carbon content. The observed C depletion in this area aligns well with this measured local reduction in hardness in the LC steel FZ (see Fig. 6b).

As shown in Fig. 8c and d, Mn, and Si compositions are significantly lower in the case of IF steel compared to Q&P steel base metal. Moreover, there are no changes in the chemical composition visible on the IF steel side. A significant depletion of C, Mn, and Si, approximately 75 μm from the FB, is observed on the Q&P steel side as indicated by arrows (see Fig. 8b-d). Within this 75 μm wide region adjacent to the FB, the Mn and Si-depleted region, the 25 μm region nearer to the FB, experiences a substantial depletion of alloying elements, while the rest of the area maintains similar Mn and Si content as the FZ. As described in the author's previous work ^[8,18], the region near the FB, characterized by a depletion in C, Mn, and Si, is termed the "halo ring". When alloyed with lower alloyed steel, the halo ring exhibits more severe C, Si, and Mn depletion due to the triggered diffusion (downhill diffusion) of these alloying elements towards the FZ. Additionally, it can be also seen that there is a potential for diffusion of C from the halo to the HAZ (see Fig. 10). This can be attributed to the higher activity (difference in chemical potential) of C caused by the variation in substitutional solute content, towards the HAZ from the halo ring. This difference in chemical potential promotes the diffusion of C from the halo ring to the HAZ, intensifying the C depletion in the halo ring. As documented in the authors' previous study ^[23] the microstructure of the halo ring was identified as upper bainite. This implies that the absence of carbide-suppressing elements such as Si, promotes the carbide formations (cementite) in the halo region, resulting in a reduced availability of carbon in solid solution and causing the area to transition into bainitic ferrite. To substantiate this, there is also a notable increase in C, Mn, and Si content (approximately 20 μm inside the FZ from the FB) as illustrated in Fig. 8b, c, and d. Additionally, our previous study ^[18] has shown that the grain boundaries in the UCHAZ are depleted in Mn and Si, this implies that these elements diffuse into the FZ from regions farther away from the HAZ through grain boundary diffusion. In summary, the width of C depleted zone and the level of C depends on the welding time, temperature, the carbon content in the materials, co-diffusion of Mn and Si, and the carbon diffusivities ^[35].

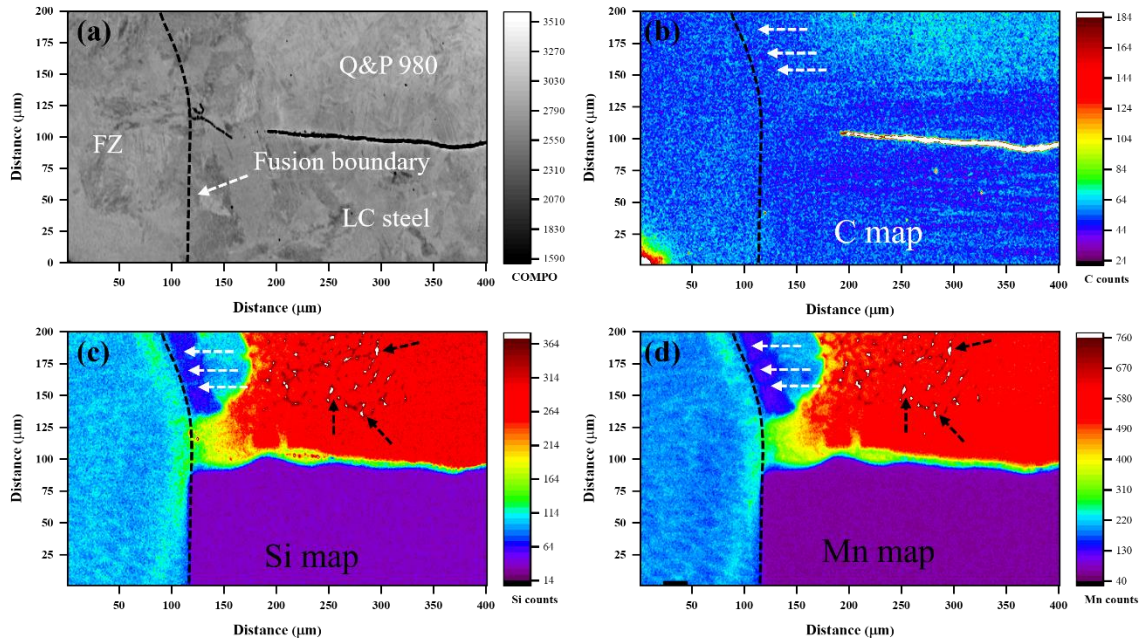


Fig. 8: LC steel sandwich weld (a) BSE SEM image; Elemental distribution map: (b) C, (c) Si, and (d) Mn.

The segregation of Mn and Si at the grain boundaries followed by the 75 μm depleted region from FB (see black arrows, which is at least $\sim 120 \mu\text{m}$ away from FB) can be seen in Fig. 8c and d. Microstructural analysis of this segregated region reveals that segregation occurs at the grain boundaries of the UCHAZ. A comprehensive examination of the elemental segregation in the UCHAZ microstructure and its effect on mechanical properties is documented elsewhere [18].

The HC steel sandwich welds, on the other hand, behaved differently than the LC steel case. Although a slight reduction in C, Mn, and Si was observed at the FB of the Q&P steel side, major elemental diffusion happened in the high carbon steel side of the joint, as shown in Fig. 9. The carbon map in Fig. 9b shows that there is no visible carbon depleted region in the Q&P steel side. However, a significant C-depleted region ($\sim 30 \mu\text{m}$) was seen on the HC steel side (see white arrows). The high C region (base metal composition) in the HC steel side starts around $110 \mu\text{m}$ away from the FB. Similarly, there is no difference in Mn and Si near the FB on the Q&P steel side (see Fig. 9c and d). Furthermore, likewise in the LC steel side of the LC steel weld, there was no visible segregation of C, Mn, and Si inside the FZ near to the FB was observed in the HC steel weld.

It is worth noting that C, Mn, and Si depletion is shifted to the high-carbon steel side. That means, alloying the Q&P steel with a higher alloyed steel causes depletion of elements in the higher alloyed steel side. On the other hand, alloying with higher alloyed steel will shift the halo to the higher alloyed steel side due to the concentration difference between the steels (downhill diffusion). This can be also seen from the hardness scan (Fig. 6c) that the difference in hardness between the halo ring and HAZ is minimal on the Q&P steel side. However, the hardness of the FZ is significantly higher than the HAZ and halo ring. This is obvious that alloying with a higher alloyed steel will increase the overall hardness of the weld FZ.

Although there is no visible C depletion observed in the Q&P steel side of the weld made with HC steel, a slight decrease in hardness is evident on the hardness map (see Fig. 6c). It is worth noting that in the Q&P steel side, C diffusion from the FB to the HAZ occurs due to the activity (uphill diffusion), resulting in a carbon depleted halo. However, this depleted C in the halo is replaced by C from the FZ, because of the concentration difference (see Fig. 10). Nevertheless, the carbon loss from the halo to the HAZ, driven by activity, is more significant than the carbon diffusion from the FZ to the halo due to concentration.

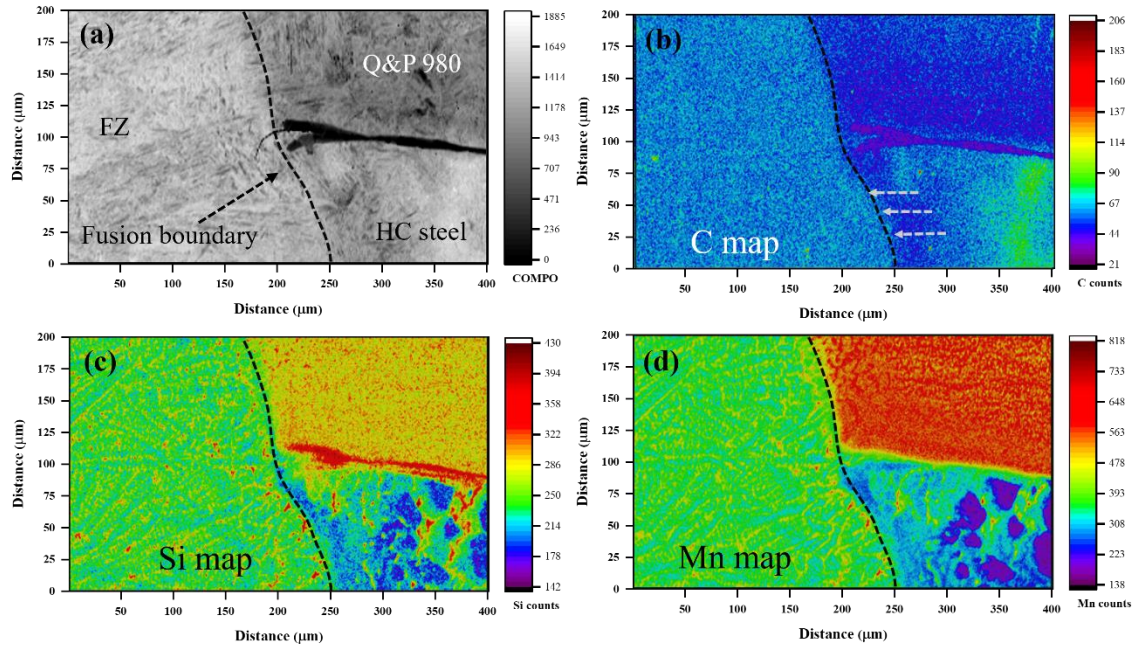


Fig. 9: HC steel sandwich weld (a) BSE SEM image; Elemental distribution map: (b) C, (c) Si, and (d) Mn.

To quantitatively understand the behavior of carbon throughout the weld area of the Q&P steel, EPMA line scans were conducted, and the results are summarised in Fig. 10. In the 3-sheet Q&P case, where no mixing with other steels happened, it is evident that the C content in the HAZ and FZ is similar. Conversely, mixing with lower alloyed steel (LC steel) reduces the overall C content in the FZ. Correspondingly, alloying with high-carbon steel increased the overall C content in the FZ. These observations align well with the hardness values presented in Fig. 6. Notably, in the LC steel case, the C content in the HAZ is slightly higher toward the base material. This observation was consistently confirmed through three repetitions of the line scans, indicating a potential uphill diffusion of C towards the HAZ due to its difference in chemical activity. It is crucial to highlight that the EPMA analysis precisely measures the amount of carbon and other alloying elements in the material. The determined C content, approximately 0.22 wt.%, demonstrates good agreement with the reported composition in Table 1.

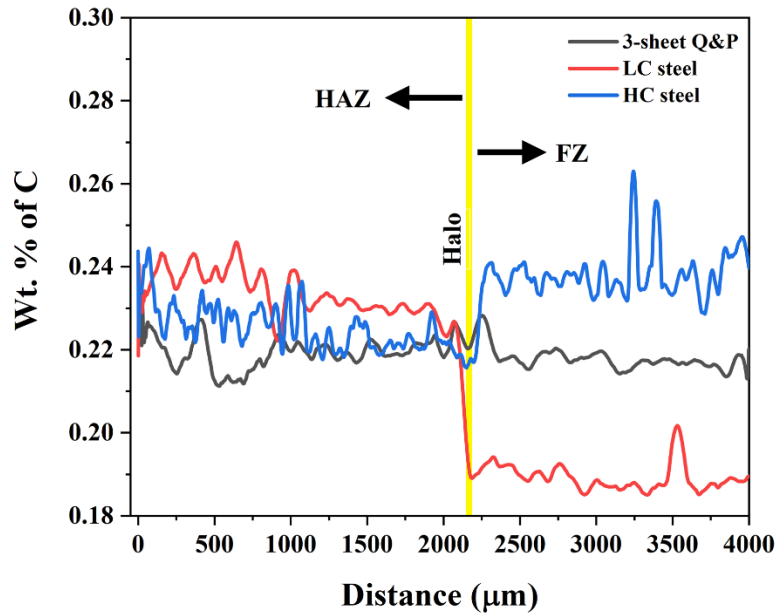


Fig. 10: EPMA line scans were taken across the FB approximately through the middle of the Q&P steel side of the weld.

The EPMA maps indicate a dissimilarity between the C, Si, and Mn content measured in the FZ and the calculated alloying elements based on each sheet's contribution to the volume fraction. The corresponding measured and calculated C, Mn, and Si contents are shown in Fig. 11. To illustrate, the calculated C content for an LC steel weld was determined by computing the volume percentage of the nugget, by considering volume contributions from each steel sheet being joined. For instance, in case of LC steel weld, the total carbon content of the weld nugget is determined by taking the volume percentage contribution of the nugget from the Q&P steel and multiplying it by the weight percent carbon in the Q&P steel. This is then added to the volume percentage contribution from the middle sheet (LC steel) multiplied by the weight percent carbon in the LC steel. To ensure accuracy, five samples were selected for each condition to validate the results, with the nugget's volume estimated from the cross-sectional area. The measured and calculated C contents with the FZ of the experimented welds are shown in Fig. 11a. In the 3-sheet Q&P weld the measured and calculated C contents (~0.21 wt.%) exhibit a close agreement with each other. However, within the FZ of the LC steel weld, the measured carbon content is notably 53% higher than the calculated value. Conversely, in the HC steel weld, the measured C content is 40% lower

than the experimental value. This discrepancy provides valuable insights into the carbon diffusion towards the FZ, elucidating the influence of concentration difference. Additionally, the reduction in carbon observed in the FB of the Q&P steel is attributed to the uphill diffusion of carbon.

The diffusion of carbon from the halo ring is related to either its chemical potential (μ) or activity (a), indicating the measure of the tendency of an atom to leave a solution. When the activity or chemical potential is low, the atoms exhibit reluctance to leave the solution. The chemical potential of a C atom, assuming an ideal solution, can be expressed by Equation 3^[36]. It's important to note that this equation offers a simplified representation of carbon's chemical potential in steels.

$$\mu_C = G_C + RT \ln X_C \quad (3)$$

Where μ_C is the chemical potential of carbon, G_C denotes the Gibbs free energy of the carbon, R stands for the universal gas constant, T is the temperature, and X_C represents the mole fraction of carbon in the solution. Thus, it is evident that the chemical potential is directly related to the temperature of the system. Additionally, the change in free energy also decreases with an increase in solute atoms^[36]. Consequently, in LC steel weld, the chemical potential of the halo is higher than that of the HAZ. Therefore, the C diffusion happens towards the HAZ from the higher activity halo to the lower activity HAZ (see Fig. 12b). Conversely, in a 3-sheet Q&P weld, the diffusion of carbon is minimal. Nevertheless, the diffusion of carbon occurs due to the difference in chemical potential aided by the temperature difference.

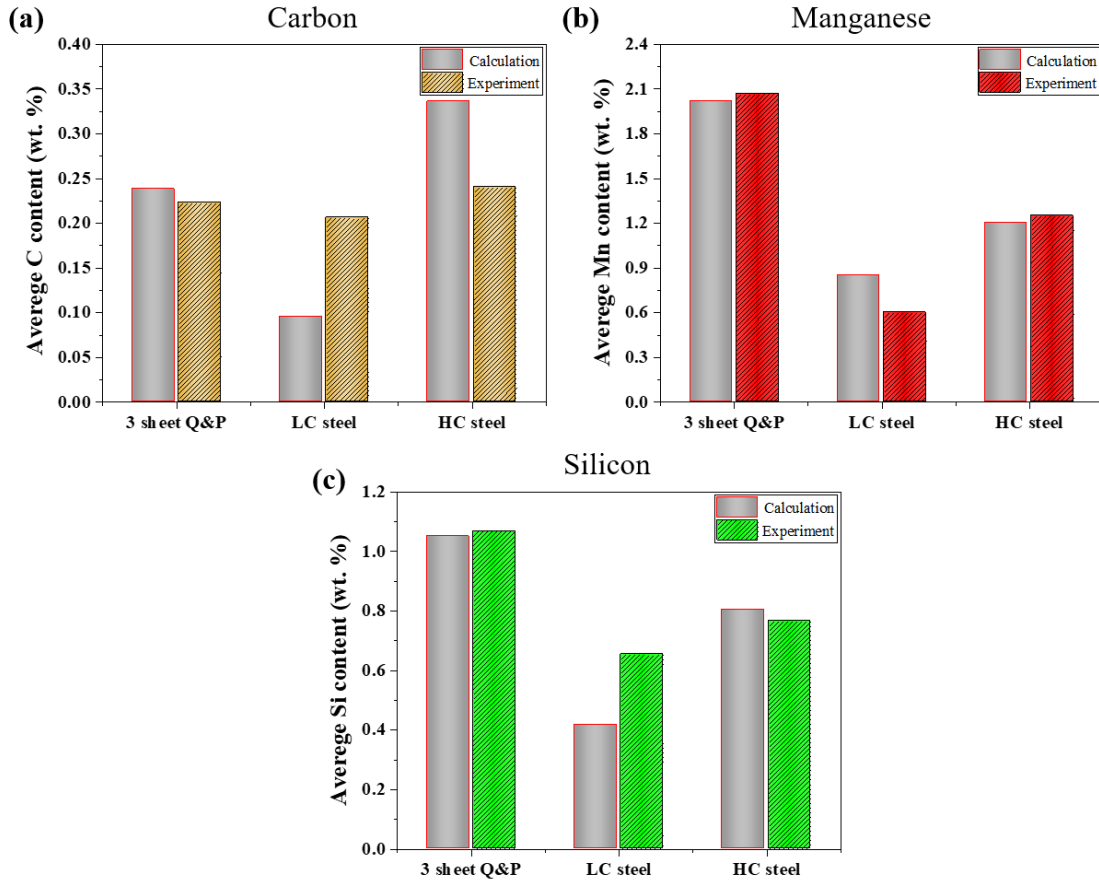


Fig. 11: Measured and experimented with elemental composition within the FZ near the FB (a) C, (b) Mn, and (c) Si.

In contrast, the Mn content in the 3-sheet Q&P and HC steel welds demonstrates a close agreement between the measured and calculated amounts (see Fig. 11b). The difference in Mn content is 2.4% and 3.5%, respectively, for the 3-sheet Q&P and HC steel welds. Conversely, a significant 41% decrease in Mn content is observed in the FZ of the LC steel weld. As illustrated in Fig. 8d, the Mn segregates near the FB, which is inside the FZ, and then Mn diffuses into the inter-dendritic regions in the UCHAZ. Huang et al. [35] reported that the diffusion of carbon in welds is linked to the precipitation of metal carbides like M_7C_3 , and $M_{23}C_6$, depending on the available carbon content in solid solution. Therefore, it can be hypothesized that the Mn may form metal carbides in combination with carbon at the grain boundaries, which need further validation.

The Si content follows a similar trend to Mn in the 3-sheet Q&P and HC steel cases. However, in the LC steel weld, there is a notable 36% increase in Si content during measurement. This increased Si content is concurrent with the observed decrease in Mn in the FZ. Examination of EPMA results presented in Fig. 7-9, reveals intriguing Si and Mn segregation in the inter-dendritic region. A comparison between 3-sheet Q&P weld with HC, and LC steel welds highlights more pronounced inter-dendritic segregation in HC and LC steel welds, which could be attributed to the lower boron content in the FZ composition ^[37]. Essentially, the reduction in boron levels during alloying with LC and HC steel in Q&P diminishes grain boundary stabilization by boron, facilitating greater diffusion of Mn and Si towards the FZ ^[24].

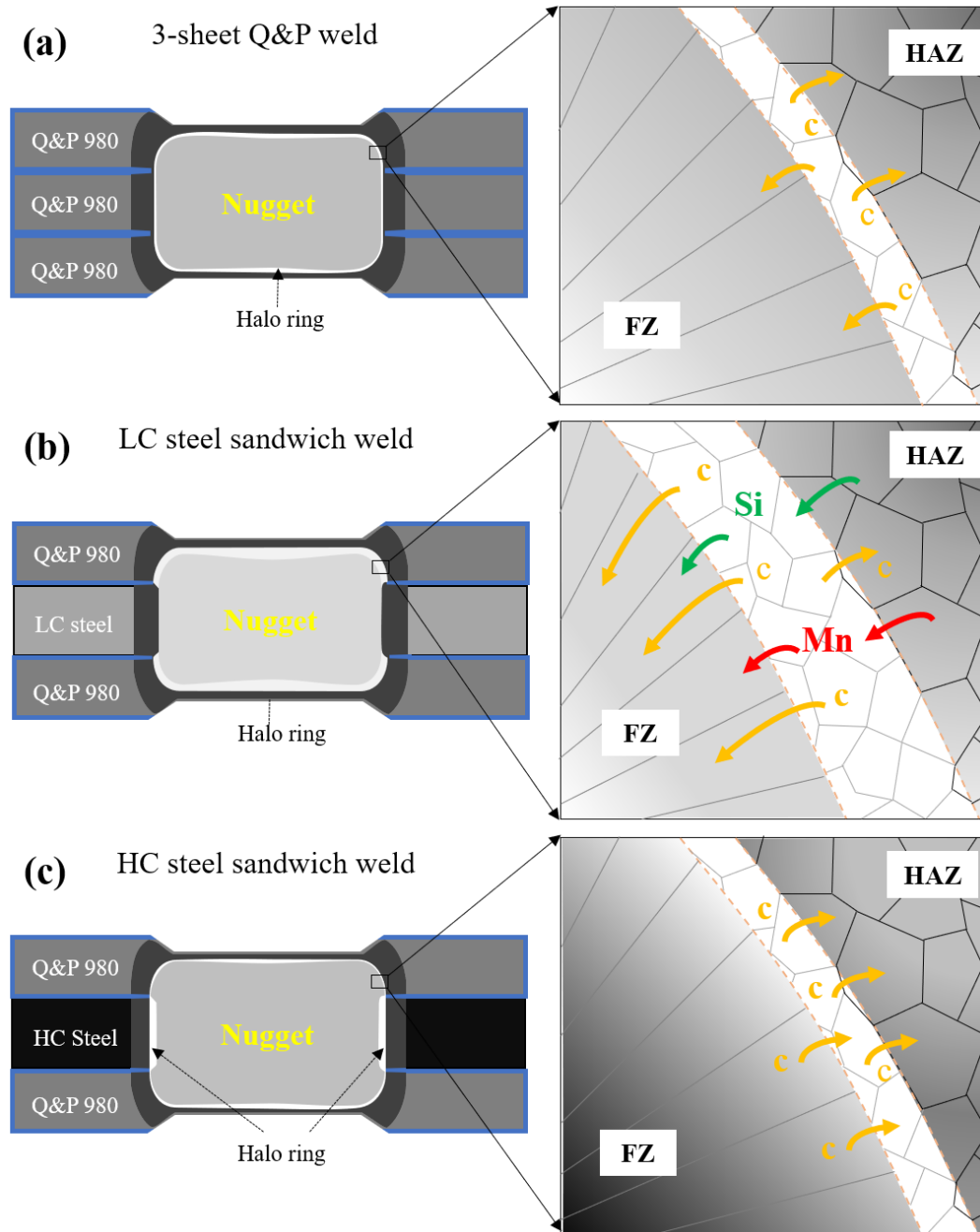


Fig. 12: Schematic diagram showing the diffusion of C, Mn, and Si in (a) 3 sheet Q&P weld, (b) LC steel sandwich weld, and (c) HC steel sandwich weld.

In summary, the diffusion of alloying elements from the halo to the FZ and HAZ of all the experimented welds are summarised in Fig. 12. The high degree of softening seen at the FB of LC steel is attributed to the combined effect of downhill diffusion of C towards the FZ from the halo

due to the concentration difference, and uphill diffusion of C to the HAZ due to the activity (see Fig. 12b). Kong et al. [38] estimated the time required for carbon depletion to happen in martensite at 320°C and 260°C to be 0.1 to 0.5 s, respectively. This estimation aligns well with the welding time employed in this study, which is 470 ms. Moreover, the temperature at the UCHAZ during welding is close to the steel's melting point, suggesting that carbon diffusion occurs even faster due to elevated temperatures. To further substantiate, the diffusion of Mn and Si also promotes this process. It is also worth noting that factors such as welding temperature, time, pressure, and the composition of the base materials all influence the C diffusion behavior during resistance spot welding. A comprehensive investigation of this phenomenon will necessitate detailed transmission electron microscopy analysis, which is the focus of ongoing research.

4. Conclusion

The effect of material chemical composition on the halo formation and its characteristics were systematically studied by alloying with lower (LC) and higher alloyed (HC) steel. A comprehensive analysis, employing EBSD analysis for microstructural assessment and EPMA analysis for chemical analysis, led to the following key findings:

1. Resistance spot welds produced by sandwiching 1.5 mm LC steel and a 1.2 mm HC steel between two sheets of Q&P980 steel sheet, revealed a significant decrease in the compositions of C, Mn, and Si in the FZ of welds made with LC steel due to the admixture of low-alloyed material in the FZ, as observed through EPMA. This change corresponded to a 46 % reduction in hardness at the FB in LC steel sandwich welds.
2. The halo formation was more prominent in welds with lesser alloyed FZ compared to those with higher alloyed FZ. The degree of softening followed a decreasing order of LC steel sandwich weld, 3-sheet Q&P weld, and HC steel sandwich weld.
3. In LC steel sandwich welds, a region of high Si and Mn segregation inside the FZ, closer to the FB, was observed on the Q&P steel side. Conversely, no significant depletion of C, Mn, and Si was observed in the HC steel sandwich weld case on the Q&P steel side. Interestingly, the halo formation shifted to the HC steel side (middle sheet) in weld made with HC steel. The halo formation in weld made with HC steel was attributed to the uphill diffusion of C from the halo to the HAZ due to the higher activity.

4. The transient softened zone can be modified by alloying with greater and lesser compositions of steel in dissimilar welded joints. Halo formation in weld made with LC steel is attributed to the combined effect of downhill diffusion of C towards the FZ from the halo due to the concentration difference, and uphill diffusion of C to the HAZ due to the activity.

Therefore, it is recommended to avoid using long welding times when working with Q&P 980 steel in both similar and dissimilar joint configuration, as halo formation is associated with diffusion of C during the welding process.

Acknowledgment

The authors would like to acknowledge the financial support from ArcelorMittal Dofasco G.P. in Hamilton, Canada, and the Natural Sciences and Engineering Research Council (NSERC). The electron microscopy was performed at the Canadian Centre for Electron Microscopy (also supported by NSERC and other government agencies).

Declaration of Competing Interest

The authors declare that they have no known competing financial interests or personal relationships that could have appeared to influence the work reported in this paper.

Credit author statement.

Dileep Chandran Ramachandran: Conceptualization, Methodology, Investigation, Data curation, Visualization, Validation, Writing - original draft. **Adib Salandari-Rabori:** Writing - review & editing. **Andrew Macwan:** Project administration, Resources, Funding acquisition, Writing - review & editing. **Elliot Biro:** Supervision, Validation, Resources, Funding acquisition, Writing - review & editing.

References

- 1 J. Speer, D.K. Matlock, B.C. De Cooman, and J.G. Schroth: *Acta Mater.*, 2003, vol. 51, pp. 2611–22.
- 2 L. Wang and J.G. Speer: *Metallogr. Microstruct. Anal.* 2013 24, 2013, vol. 2, pp. 268–81.
- 3 Y. Zhang, W. Xu, G. Zhang, W. Tao, and S. Yang: *Metall. Mater. Trans. A Phys. Metall. Mater. Sci.*, 2022, vol. 53, pp. 794–809.
- 4 V. Vijayan, S.P. Murugan, S.G. Son, and Y. Do Park: *J. Mater. Eng. Perform.*, 2019, vol. 28, pp. 7514–26.
- 5 B. Figueredo, D.C. Ramachandran, A. Macwan, and E. Biro: *Weld. World*, 2021, vol. 65, pp. 2359–69.
- 6 Y. Jing, Y. Xu, D. Wang, J. Li, Y. Yu, and L. Lu: *Mater. Charact.*, 2023, vol. 202, pp. 113041–55.
- 7 S. Yan, X. Liu, T. Liang, J. Chen, and Y. Zhao: *Steel Res. Int.*, 2019, vol. 90, pp. 1800257–67.
- 8 D.C. Ramachandran, B. Figueredo, O. Sherepenko, W. Jin, Y. Do Park, and E. Biro: *J. Manuf. Process.*, 2022, vol. 75, pp. 320–30.
- 9 Y. Ma, A. Takikawa, J. Nakanishi, K. Doira, T. Shimizu, Y. Lu, and N. Ma: *Mater. Des.*, 2021, vol. 201, p. 109505.
- 10 S.T. Wei, R.D. Liu, D. Lv, L. Lin, R.J. Xu, J.Y. Guo, K.Q. Wang, and X.F. Lu: *Sci. Technol. Weld. Join.*, 2015, vol. 20, pp. 20–6.
- 11 P. Russo Spena, M. De Maddis, G. D’Antonio, and F. Lombardi: *Metals (Basel)*, 2016, vol. 6, p. 270.
- 12 P.R. Spena, M. De Maddis, F. Lombardi, and M. Rossini: *Mater. Manuf. Process.*, 2016, vol. 31, pp. 291–9.
- 13 M. Pouranvari, S.M. Mousavizadeh, S.P.H. Marashi, M. Goodarzi, and M. Ghorbani: *Mater. Des.*, 2011, vol. 32, pp. 1390–8.
- 14 D.S. Safanama, S.P.H. Marashi, and M. Pouranvari: *Sci. Technol. Weld. Join.*, 2012, vol. 17, pp. 288–94.
- 15 V.H. Baltazar Hernandez, M.L. Kuntz, M.I. Khan, and Y. Zhou: *Sci. Technol. Weld. Join.*, 2008,

- vol. 13, pp. 769–76.
- 16 A. Chabok, E. van der Aa, and Y. Pei: *Mater. Sci. Eng. A*, 2020, vol. 788, p. 139501.
 - 17 M. Pouranvari and S.P.H. Marashi: *Sci. Technol. Weld. Join.*, 2013, vol. 18, pp. 361–403.
 - 18 D.C. Ramachandran, O.T. Betiku, M. Shojaee, A. Salandari-Rabori, A.R.H. Midawi, J.U. Kim, R. Bakhtiari, A. Macwan, and E. Biro: *Mater. Charact.*, 2023, vol. 206, p. 113383.
 - 19 T. Taniguchi, T. Mizutani, H. Horikawa, S. Furusako, and S. Kodama: *J. Manuf. Process.*, 2024, vol. 117, pp. 1526–6125.
 - 20 S.M. Manladan, Y.J. Jang, and Y. Do Park: *J. Mater. Res. Technol.*, 2023, vol. 24, pp. 4756–61.
 - 21 Y. Jing, Y. Xu, D. Wang, L. Lu, J. Li, and Y. Yu: *Mater. Sci. Eng. A*, 2022, vol. 843, p. 143130.
 - 22 Y. Zhang, W. Xu, G. Zhang, W.U. Tao, and S. Yang: *Metall. Mater. Trans. A* 2021, 2022, pp. 1–16.
 - 23 D.C. Ramachandran, A. Salandari-Rabori, A. Macwan, and E. Biro: *Metall. Mater. Trans. A Phys. Metall. Mater. Sci.*, 2024, vol. 55, pp. 4298–4303.
 - 24 M. Amirthalingam, E.M. van der Aa, C. Kwakernaak, M.J. M. Hermans, and I.M. Richardson: *Weld. World*, 2015, vol. 59, pp. 743–55.
 - 25 D.C. Ramachandran, A. Salandari-Rabori, A.R.H. Midawi, A. Macwan, and E. Biro: *ISIJ Int.*, 2024, vol. 64, pp. 1178–84.
 - 26 P. Russo Spina, M. De Maddis, G. D’Antonio, and F. Lombardi: *Metals (Basel)*, 2016, vol. 6, p. 270.
 - 27 O. Sherepenko, O. Kazemi, P. Rosemann, M. Wilke, T. Halle, and S. Jüttner: *Metals (Basel)*, DOI:10.3390/met10010010.
 - 28 O. Sherepenko and S. Jüttner: *Weld. World*, 2019, vol. 63, pp. 151–9.
 - 29 T. Kasuya and N. Yurioka: *Weld. Res. Suppl.*, 1993, vol. 6, pp. 263-s-268-s.
 - 30 AWS D8 Committee on Automotive Welding: *Test Methods for Evaluating the Resistance Spot Welding Behaviour of Automotive Sheet Steel Materials*, 2012.
 - 31 AWS: *AWS D8.1M:2007 Specification for Automotive Weld Quality-Resistance Spot Welding of Steel*, 2007.

- 32 J.E. Gould, S.P. Khurana, and T. Li: *Weld. J. (Miami, Fla)*, 2006, vol. 85, pp. 111s-116s.
- 33 D.C. Ramachandran, A.R.H. Midawi, M. Shojae, O. Sherepenko, H. Ghassemi-Armaki, and E. Biro: *Materialia*, 2022, vol. 26, p. 101644.
- 34 P. Eftekharimilani, E.M. van der Aa, M.J.M. Hermans, and I.M. Richardson: *Weld. World*, 2017, vol. 61, pp. 691–701.
- 35 M.L. Huang and L. Wang: *Metall. Mater. Trans. A Phys. Metall. Mater. Sci.*, 1998, vol. 29, pp. 3037–46.
- 36 D.A. Porter, K.E. Easterling, and K.E. Easterling: *Phase Transformations in Metals and Alloys*, vol. 15, 2009.
- 37 N.D. Raath, D. Norman, I. McGregor, R. Dashwood, and D.J. Hughes: *Metall. Mater. Trans. A* 2017 486, 2017, vol. 48, pp. 2900–14.
- 38 H. Kong, Q. Chao, M.H. Cai, E.J. Pavlina, B. Rolfe, P.D. Hodgson, and H. Beladi: *Mater. Sci. Eng. A*, 2017, vol. 707, pp. 538–47.